PCCP

Accepted Manuscript

ROYAL SOCIETY OF CHEMISTRY

www.rsc.org/pccp

Carries mobility of MoS_2 nanoribbons with the edge chemical modification

Jin Xiao[1], Mengqiu Long[1,2*], Mingjun Li[1], Xinmei Li[1], Hui Xu[1*], and Kwoksum Chan[2,3*]

[1]*Institute of Super-microstructure and Ultrafast Process in Advanced Materials, School of Physics and Electronics, Central South University, Changsha 410083, China*

[2]*Department of Physics and Materials Science, City University of Hong Kong, Hong Kong, China*

[3]*City University of Hong Kong Shenzhen Research Institute, Shenzhen, China*

*E-mail: mqlong@csu.edu.cn, cmpxhg@csu.edu.cn, apkschan@cityu.edu.hk

Abstract

We have investigated the electronic structures and carrier mobilities of MoS_2 monolayer sheet and armchair nanoribbons with chemical modification using density functional theory combined with Boltzmann transport method with relaxation time approximation. It is shown that the hole mobility (96.62 $cm^2V^{-1}s^{-1}$) in monolayer sheet is about twice of electron mobility (43.96 $cm^2V^{-1}s^{-1}$). The charge mobilities in MoS_2 armchair nanoribbons can be regulated by edge modification owing to the electronic structures changed. In pristine armchair nanoribbons, the electron mobility is about 30 $cm^2V^{-1}s^{-1}$ and the hole mobility is about 25 $cm^2V^{-1}s^{-1}$. When the edges are terminated by H or F atoms, the hole mobility will enhance obviously even ten times of that in pristine ribbons, and the electron mobility is comparable with that in MoS_2 sheet.

***Keywords*:** Molybdenum disulfide; Density functional theory; Electronic structure; Chemical modification; Carries mobility;

Introduction

Two-dimensional atomically-thick materials have attracted intensive attention owing to their unique physical properties and potential applications in nanoscale devices [1-9]. Layered transition-metal dichalcogenides (TMDs) which are important two-dimension materials, MX_2 (M=Mo, W, Ta, or Nb, and X= S, Se, or Te) are also considered as promising electronic and optoelectronic materials [9-15] and the successful syntheses of these materials have already been reported [16-20]. MoS_2, an important representative member of the TMD family, arouses many researchers' strong interest in the materials in recent years [19-23]. The monolayer MoS_2 is a direct band gap semiconductor with a band gap of 1.9 eV [23, 24] and the room-temperature current on/off ratio can be as high as 1×10^8 [13]. Owing to the breaking of the inversion symmetry, very obvious spin-orbit interaction effect is found around the high-symmetry k-points of the Brillouin zone with a spin-orbit splitting as high as 150 meV [25-27] according to some theoretical studies and around 160 meV [28-31] according to some experimental studies. Utilizing this effect, the optical generation of valley polarization is achieved with the polarized photoluminescence technique in monolayer MoS_2 [28-33].

Recently, the mobilities (μ) of two-dimensional materials attract many researchers' attentions [2, 34-48]. Some measurements showed that the room-temperature mobility of bulk MoS_2 is in the range 200-500 $cm^2V^{-1}s^{-1}$ [43]. The field effect mobility of atomically thin MoS_2 FET was reported to vary from 0.5 to 800 $cm^2V^{-1}s^{-1}$ [13, 44-48]. By using a femto-second pump-probe technique to study the charge carriers, a carrier lifetime of 100±10 picosecond and a carrier diffusion coefficient of 20±10 cm^2/s are obtained, which correspond to a mobility of 800 $cm^2V^{-1}s^{-1}$ and a diffusion length of 450 nm[48]. The presence of high-K dielectrics in some devices can enhance the mobilities [46], to values reaching ~200 $cm^2V^{-1}s^{-1}$ [13]. Radisavljevic B. and Kis A.[46] reported that phonon scattering shows a weaker than expected temperature dependence (μ follows a $T^{-\gamma}$ dependence with $\gamma = 0.55–0.78$) when temperature above ~100K, and the mobility at 4 K is 174 $cm^2V^{-1}s^{-1}$ and it reaches 63 $cm^2V^{-1}s^{-1}$ at 240 K.

By confinement of the two dimensional bulk materials, one-dimensional materials can be created with different properties. For example, the carrier mobility of one-dimensional graphene ribbons is significantly lower than that of a graphene sheet owing to the loss of the massless Dirac Fermion characteristics [34, 49]. One-dimensional MoS_2 structures, such as nanoribbons [50] and nanotubes[16-19] have also been synthesized, and the mobilities of these structures have attracted the researchers' attention [42, 51]. Nevertheless, there are few reports about the mobilities of MoS_2 nanoribbons with edge modification.

In this study, by using first-principles calculations and the deformation potential theory, we investigate the intrinsic mobility of MoS_2 materials due to the acoustic phonon scattering mechanism. The carrier mobility is calculated by the Boltzmann transport equation (BTE) method. The sheets and nanoribbons, especially the chemical modifications on the ribbon's edges, are considered in the calculations. Our results show that the electron structures and the mobilities of MoS_2 ribbons are sensitive to edge modification, and hydrogen atom termination will slightly change their mobility while the halogen atom termination will obviously enhance the hole mobility (μ_h). This implies the electronic properties and the mobilities of MoS_2 nanoribbons can be regulated by chemical modification.

Methods

Theoretically, there are two models for chare transport: hopping and band-like. The former describes the thermally activated hopping of a charge carrier over a barrier, which results in a mobility, which increases with temperature owing to the increased thermal activation. The hopping model has been described by the Marcus theory for many organic materials. The latter model describes a delocalized charge undergoing coherent motion, which results in a mobility, which decreases with temperature owing to increased phonon scattering [38, 52]. Experiments find that the mobility of MoS_2 sheet decreases with temperature [46]. So the band-like model is more appropriate in MoS_2 than the Marcus electron transfer theory. Our method is based on the band-like model.

In this paper, the carrier mobility is calculated by the BTE method beyond the effective mass approximation which is used to predict the mobility of semiconductor nanometerials, like graphene, carbon nanotubes etc [2, 34-38]. Within the BTE method, the carrier mobility μ in the relaxation time approximation can be expressed as [Ref. 2 and 54]:

$$\mu^{e(h)} = \frac{e}{k_B T}\frac{\sum_{\mathrm{i}\in CB(VB)}\int \tau(i,\vec{k})v^2(i,\vec{k})\exp\left[\mp\frac{\varepsilon_i(\vec{k})}{k_B T}\right]\mathrm{d}\vec{k}}{\sum_{\mathrm{i}\in CB(VB)}\int \exp\left[\mp\frac{\varepsilon_i(\vec{k})}{k_B T}\right]\mathrm{d}\vec{k}} \qquad (1)$$

Where the minus (plus) sign is for electron (hole). $\tau(i,\vec{k})$ is the relaxation time, $\varepsilon_i(\vec{k})$ and $v(i,\vec{k})$ are the band energy and the component of the group velocity of the $\vec{k}$ state of the *i*th band, respectively. The summation of the band was carried out over the VB for hole and CB for electron. Furthermore, the integration with respect to the $\vec{k}$ states covers the first Brillouin zone (BZ).

In order to obtain the mobility, three key quantities ($\tau(i,\vec{k})$, $\varepsilon_i(\vec{k})$ and $v(i,\vec{k})$) must be determined. As the wavelengths of the thermally activated electrons or holes at room temperature in inorganic semiconductors, which are much larger than the lattice constant, is close to those of the acoustic phonon modes in the center of the first BZ, the electron−acoustic phonon coupling dominates the scattering at the low energy regime[39-41], which can be calculated effectively by the deformation potential (DP) theory proposed by Bardeen and Shockley[53]. Accordingly, the relaxation time $\tau(i,\vec{k})$ based on the DP theory can be expressed as [2, 38]:

$$\frac{1}{\tau(i,\vec{k})} = k_B T\frac{2\pi E_i^2}{\hbar C}\sum_{k'\in\mathrm{BZ}}\left\{\left[1-\frac{\vec{v}(i,\vec{k}')}{\vec{v}(i,\vec{k})}\right]\delta\left[\varepsilon(\vec{k})-\varepsilon(\vec{k}')\right]\right\} \qquad (2)$$

Here the delta function implies that the scattering process is elastic and occurs between states with the same band index. E_i is the DP constant of the *i*-th band, and C is the elastic constant.

The band energy $\varepsilon_i(\vec{k})$ is calculated using the Vienna *ab-initio* simulation package

(VASP) [54]. The $\vec{k}$-mesh is chosen as 1×1×300 for the ribbons and 65×65×1 for the sheets, which are fine enough to give converged relaxation times and mobilities. The generalized gradient approximation (GGA) [56] with the Perdew-Wang (PW91) [57] exchange correlation function is used with the plane-wave cutoff energy set at 400 eV for all calculations. The criterion of convergence is that the residual forces are less than 0.005 eV/Å and the change of the total energy is less than 10^{-6} eV. The vacuum space between two adjacent NRs is set to be at least 10Å to eliminate the interactive effect between the two NRs. The group velocities of the electron and hole carriers can be obtained from the gradient of the band energy $\varepsilon_i(\vec{k})$ in $\vec{k}$-space according to $\upsilon(i,\vec{k}) = \nabla\varepsilon_i(\vec{k})/\hbar$.

Results and Discussion

The atomic structure of the material is shown in Fig. 1a. In order to illustrate the atomic arrangements for carrier conduction along the armchair (x) and zigzag (y) directions, an orthogonal supercell which is covered by green shadow in Fig. 1a, is shown. The structure of an armchair ribbon is shown in Fig. 1b. We use the number of atomic chain (*Na*) to describe the width of the ribbon. Two kinds of edge modification were investigated: H atom termination (H-termination) and F atom termination (F-termination). The pristine ribbon is also investigated as a reference.

Firstly, the electronic structure and the acoustic phonon-limited mobility in monolayer MoS_2 are investigated. And the band structure and the first BZ of monolayer MoS_2 are shown in Fig. 2a and b respectively. For monolayer MoS_2 sheets, the K point (with fractional reciprocal coordinates: −1/3, 2/3) defined in reciprocal lattice of the primitive cell is folded into the (0, 1/3) point of the Γ-Ψ branch in the first BZ of the supercell (see Fig. 2b). There are two peaks around the top of the valence band, but only one band valley around the bottom of the conduction bands. The band structure is the same as in *Yong qing*'s report [42].

The variation of the total energy (E) with a uniaxial strain (δ) applied along the x and y directions are shown in Fig. 2c. Based on these energy-strain curves, the in-plane stiffness C^{2D} can be obtained and the C^{2D} along the x and y directions are 131.311 and 131.473 N/m respectively. The C^{2D} in our calculation are consistent with the *Yong qing*'s report (127.44 and 128.16 N/m). In general, the three-dimensional (3D) Young's modulus can be estimated as $C^{3D}= C^{2D}/t_0$. By assuming a finite thickness of (t_0 = 0.65 nm) for the 2D MoS_2 sheet, the Young's modulus amount are 202.02 and 202.27 GPa, respectively, which are in good agreement with the experimental value of 270 ± 100 GPa [58, 59]. Fig. 2d shows the shift of the band edges as a function of the strain along the x and y directions. Through dilating the lattice along x and y directions, the DP constant E_1 is then calculated as $dE_{edge}/d\delta$, equivalent to the slope of the fitting lines, where E_{edge} denotes the energy of the conduction or valence band edge. For the conduction bands, there is just one band edge which is located at the K point. The E_1 of electron along the x and y directions are -10.80 and -10.68 eV respectively which are the same as those reported by *Yong qing* [42]. But there are two band edges for the valance bands: one is located at the K point (the E_1 of hole along the x and y directions are -5.28 and -5.22 eV respectively which is the same as that reported by *Yong qing* [42]); the other one is located at the Γ point (the E_1 along the x and y directions are 1.31 and 0.82 eV respectively).

Based on the obtained energy band spectrum, the values of E_1 and C^{2D}, the acoustic-phonon-limited relaxation time (using *Eq 2*) and the mobility (using *Eq 1*) at room temperature (300 K) are obtained, as shown in Table 1. The electron mobilities are 41.27 (the x direction) and 43.96 (the y direction) $cm^2V^{-1}s^{-1}$. The hole mobilities are 96.62 (the x direction) and 64.19 (the y direction) $cm^2V^{-1}s^{-1}$ for the K point, 3079.39 (the x direction) and 4973.83 (the y direction) $cm^2V^{-1}s^{-1}$ for the Γ point. If the BZ is divided into two parts: one includes the Γ point peak (signed as BZΓ); the other excludes the Γ point peak (signed as $\overline{\mathrm{BZ\Gamma}}$, which includes K point peak), the total relaxtion time(τ) can be determined as:

$$\frac{1}{\tau(i,\vec{k})} = k_B T\,\frac{2\pi E_i^2}{\hbar C}\sum_{k'\in \mathrm{BZ\Gamma}}\left\{\left[1-\frac{\vec{v}(i,\vec{k'})}{\vec{v}(i,\vec{k})}\right]\delta\left[\varepsilon(\vec{k})-\varepsilon(\vec{k'})\right]\right\} + k_B T\,\frac{2\pi E_i^2}{\hbar C}\sum_{k'\in \overline{\mathrm{BZ\Gamma}}}\left\{\left[1-\frac{\vec{v}(i,\vec{k'})}{\vec{v}(i,\vec{k})}\right]\delta\left[\varepsilon(\vec{k})-\varepsilon(\vec{k'})\right]\right\} = \frac{1}{\tau_\Gamma(i,\vec{k})}+\frac{1}{\tau_K(i,\vec{k})} \qquad (3)$$

We can obtian the total hole relaxtion time, which equals τ_K. Then following *Eq 1,* the hole mobility can be obtained. The μ_h of a MoS_2 sheet are about 96.62 (the x direction) and 64.19 (the y direction) $cm^2V^{-1}s^{-1}$. These values are smaller than the mobilities predicted by the effective mass method [42], owing to the more band detials considered in the BTE method. Our study shows that μ_e is about a half of μ_h. Our mobility results are in very good agreement with a recent indirect measurement based on the Hall effect for thin flake MoS_2 reported by *Zhang Yijin* et al [60]. It showed that μ_h (86 $cm^2V^{-1}s^{-1}$) is twice the value of μ_e (44 $cm^2V^{-1}s^{-1}$)[60]. Owing to the var de waals interation, the top of the valance band located at the K and Γ points in monolayer MoS_2 will shift to the Γ point in the multilayer material [61]. So the μ_h in the multilayer and bulk material will be mainly determined by the Γ points and is much larger than that of the monolayer material. And the mobility as a function of tempeture is shown in Fig 3. It can be found that the mobilies of MoS_2 sheet decrease with a T^{γ} dependence with γ=1.05, 1.25, 1.37 and 1.30 for the holes and electrons in the x and y directions, respectively. In experment, phonon scattering shows a weaker than expected temperature dependence (γ = 0.55–0.78) when temperature is above ~100K. But when termperature is above ~200K, phonon scattering plays a major role in charge mobility, and mobility depends on T as $\mu\sim T^{1.4}$ [46], which is in good agreement with our calculation.

In MoS_2 sheet, the states near the Γ point experience a strong interlayer coupling effect, as a result of the combination of the antibonding p_z-orbitals on the S atoms and *d* orbitals on the Mo atoms. Coming from the localized *d* orbitals on the Mo atoms, the states at the K-point are mainly located in the middle of the S–Mo–S sandwich structure and relatively unaffected by the interlayer coupling [61]. And there is a conduction valley located on the K-point, which is similar to graphene. In graphene, the electron at the K-point is considered as quasi free π electron and the mobility can be up to 3×10^5 $cm^2V^{-1}s^{-1}$ [38]. However, in MoS_2 sheet, the π electron is located on Mo atoms and restricts the electron's movement. When the valance electron is excited to the conduction bands, there is a corresponding hole carrier. Owing to the fact that there are two valance band peaks, the hole carriers can be classified as the "σ" hole (located on Γ-point) and the “π” hole (located on K-point). In our calculation, the “σ” hole can move much faster than “π” hole. The reason can be found from the composition of the valance band. The valance band near the K-point is the combination of the *d* orbitals on the Mo atoms, which are bad for hole’s movement. And the valance band near the Γ-point is the combination of the antibonding p_z-orbitals on the S atoms and the *d* orbitals on the Mo atoms, which are good for the hole’s movement. In MoS_2, the electron being excited at the K point is easier than at the Γ point owing to the direct gap at the K point. Then it leads to the “π” hole being the major component of hole. Since the mobility is always decided by the slower one, the migration speed of the “π” hole determines the mobility of a MoS_2 sheet.

Next, we invesitage the μ of MoS_2 nanoribbons. As the zigzag MoS_2 nanoribbons are metallic, here we only consider the semiconducting armchair MoS_2 nanoribbons, which are classified by the number of Mo−S dimer lines (N) across the ribbon width, as shown in Fig. 1b. A series of armchair nanoribbons with widths in the range $7 \leqslant N \leqslant 16$ (from 1.0 to 2.4 nm) are calculated. It is well-known that edge states exist in MoS_2 nanoflakes and dominate their catalytic performance. Thus, we expect different edge modifications can affect the properties of the nanoribbons and we threfore investigate the following three kinds of edge modfication in the present study, pristine, H-termination and F-termination. The energy bands for these three edge modifications are shown in Fig. 4, in which it can be noted that there are the same deep energy bands. The differences in the band structures can be found between -0.3 and 1.5 eV. There are ten bands(4 valance bands and 6 conduction bands) for the pristine ribbon and 4 bands (2 valance bands and 2 conduction bands) for the H-termination and F-termination ribbons, and the energy bands of the H-termination ribbon is similar to those of the pristine ribbon. Both of them are direct gap semcoductors at the Γ points, and their energy gaps are oscillating aroud 0.55 eV with respect to the width. However, for the F-ternimation, the direct gap shifts to the K point, and the energy gap increases to about 0.95 eV.

For the 1D case, the stretching modulus is defined as $C^{1D} = [\partial^2 E / \partial \delta^2] / L_0$, where the uniaxial strain δ is applied along the ribbon direction, and L_0 is the lattice constant of the optimized ribbon, which is shown in Fig. 5a. Owing to the additional unpaired electrons, the Mo-S bonds at the ribbon edges are shorter than the bonds of at ribbon's center, which lead to a small L_0 in pristine ribbons. For edges modified by H or F atoms, the L_0 is almost constant for different lattice lengths of the monolayer MoS_2 ribbon along the x direction (the black dashed line in Fig. 5a). Fig. 5b shows that C^{1D} increases continuously with N for all three kinds of ribbons. Considering the same width (W_0) for these three ribbons, the effective C^{2D} for the ribbon can be obtained as C^{1D}/W_0, which is between 102.8 and 116.4 N/m for pristine ribbons (between 100.7 and 113.6 N/m for the H-termination, and between 102.8 and 116.4 N/m for the F-termination). Compared with the 2D sheet, the phonon spectrum of the nanoribbons broadens toward the high-frequency region owing to the phonon mode quantization and the occurrence of edge phonon modes, which leads to the softening of the lattice modes and the reduction of the elastic modulus[42].

Fig. 5c,d show the the DP constant E_1 of electrons and holes due to the quasi-static deformation of the ribbon. It can be noted that the $|E_1|$ of both electrons and holes are increasing with N for the three kinds of ribbons. For a spectific Na, the largest hole $|E_1|$ is found in the F-termination ribbons which is about 2 eV higher than the pristine ribbons. The H-termination ribbons have the smallest hole $|E_1|$ which ranges between 2 eV and 3.5 eV. But for the electron $|E_1|$, the smallest one is in the F-termination ribbons, which is smaller than 1 eV; the largest one is in pristine ribbons, which is about twice of that of H-termination. $|E_1|$ of hole is about five times larger than that of electron in F-termination ribbons. In pristine ribbon, $|E_1|$ of hole is about 1 eV larger than that of electron. The difference of $|E_1|$ between electrons and holes is almost zero in H-termination ribbons. These results show tht E_1 can be modified by edge modification in MoS_2 ribbons.

The room temperature μ for the ribbons are shown in Fig. 6, and the μ of the 2D sheet, represented by the horizontal dashed orange line, is also plotted for comparison. The μ_e and μ_h in prinstine ribbons oscillate between 25 and 35 $cm^2V^{-1}s^{-1}$ vary with changing the width of the nanoribbons, respectively. The mobility in the H-termination ribbons initially oscillates with the width of the nanoribbons and then levels off to a value of 44.80 and 93.95 $cm^2V^{-1}s^{-1}$ for electrons and holes, which are close to the mobility of the 2D sheet (μ_e :41.27 $cm^2V^{-1}s^{-1}$; μ_h: 96.62 $cm^2V^{-1}s^{-1}$). The H-termination ribbons can be divided into three groups which show smooth dependence on the width of ribbon N within each group. The first group is ribbons with the ribbon width $Na = 3p + 1$ (p is an integer) which has the largest μ_e. The $Na = 3p + 2$ group has the largest μ_h, and the $3p$ group has the smallest μ_e and μ_h. The μ_e of F-termination ribbons moves close to that of the 2D sheet with the increase of the width of the nanoribbons. The μ_h in the F-termination ribbon initially can be above 10^3 $cm^2V^{-1}s^{-1}$, even with a maximum up to 2413.85 $cm^2V^{-1}s^{-1}$, for some smaller ribbon widths < 11, and then descreases with the increase of the width of the nanoribbons when the width is above 11. Nevertheless, the μ_h in the F-termination ribbons can still be as high as to 425.20 $cm^2V^{-1}s^{-1}$ (for Na=16).

To understand the behavior of μ for different edge modifications in MoS_2 nanoribbons, we analyze the band decomposed charge density at the edge of bands, as shown in Fig. 7. Since the same nanoribbons with the edge modification have a similar electronic character, the $Na = 10$ nanoribbon is chosen as a representative for the analysis. It can be noted that the edge of the conduction bands is entirely located at atoms of the ribbon edges. The edge of valance bands is mainly located at atoms of the ribbon edges of pristine and H-termination ribbons, and entirely located at atoms of the ribbon edges in F-termination ribbons. The band decomposed charge density in the F-termination ribbons has the mirror symmetry. For pristine ribbons, two valance bands (v_1 and v_2 in Fig. 7a) and four conduction bands (c_1, c_2, c_3 and c_4 in Fig. 7a) are considered. Atomic orbital analysis shows that all these states are mainly composed of Mo 4d manifolds and the edge S atoms provide little contributions for the conduction bands (c_1 and c_2 in Fig. 7a). The conduction bands (c_1 and c_2 in Fig. 7a) are hybridization orbits with mixed 4d and 2p orbits. For the H-termination ribbons, the valance bands are similar to those in the pristine ribbons; and the difference in valance bands is that the plane states located at -0.25~-0.3 eV (as shown in Fig. 4a), those states are composed of S 2p orbits in pristine ribbons, are vanished in the

H-termination ribbon. There are two conduction degenerate bands (c_1 and c_2 in Fig. 7b) below 1.5 eV in H-termination ribbons. And atomic orbital analysis shows that the conduction bands are composed of Mo 4*d* manifolds (*d*yz, *d*z^2 and *d*x^2-y^2), S 2*p* and H 1*s* orbits. For F-termination, there are two double degenerate bands (v_1, v_2 and c_1, c_2 in Fig. 7c) around the Fermi level, and the atomic orbital analysis shows that F 2*p* manifolds account for an important proportion of all these states. Owing to the F 2*p* states, the electronic structures around the Fermi level brings a major change: the energy gap shifted from the Γ to the Z point.

From the band structure, we can find states near the Fermi level which have parabolic dispersion. So the effective mass (m^*) can obtained by $\hbar^2[\partial^2\varepsilon(\mathrm{k})/\partial \mathrm{k}^2]^{-1}$, as shown in Fig. 8a,b. The electron effective mass initially oscillates with the width of the nanoribbons and then levels off to about 1.3 m_e (m_e is the mass of free electron) in the ribbons with three kinds off edge modifications. In the F-termination ribbons, the hole effective mass also initially oscillates with the width of the nanoribbons and then levels off to a value of 1.5 m_e. There are three families of the hole effective mass showing smooth trends within each family. The 3*p* family have the largest hole effective mass both for the pristine and H-termination ribbons. The 3*p*+2 family have the smallest hole effective mass for the H-termination ribbons and the 3*p*+1 family have the smallest hole effective mass for the prinstine ribbons. The osillatory behavior of the hole effective mass gives rise to an oscillating μ_h. The mobility determined from the effective mass using the experssion $\mu = e\hbar^2 \mathrm{C}[(2\pi \mathrm{k_B T})^{\frac{1}{2}}|m^*|^{\frac{3}{2}}E_1^2]^{-1})$ is shown in Fig. 8c,d. The μ_e in the pristine ribbon oscillates aroud 60 cm^{2}V^{-1}s^{-1} which is close to the μ_e in monolayer MoS_2 reported by [42]. The μ_h in the pristine ribbons has oscillations with a period of 3. The smallest mobility is found in the 3*p* family and the largest mobility is found in the 3*p*+1 family. The μ_e of the H-termination ribbon initially oscillates with the width of the nanoribbons and then levels off to about 80 cm^{2}V^{-1}s^{-1}. There are three families of μ_h in H-termination ribbons showing smooth trends within each family, with the 3*p* family having the smallest mobility and 3*p*+2 family having the largest mobility. The μ_e in F-termination slowly increases from 20

$cm^2V^{-1}s^{-1}$ to 30 $cm^2V^{-1}s^{-1}$ with $7\leqslant N\leqslant 16$. But the μ_h in F-termination ribbons is up to about 10^3 $cm^2V^{-1}s^{-1}$. The mobility predicted by the effective mass method is agreement with that predicted by the BTE method, except the μ_e in pristine ribbons which is larger than that in F-termiantion. In a word, both of effective mass and BTE method suggest that the edge modification in MoS_2 ribbons can regulate the mobility.

From the mobilities of pristine, H-termination and F-termination systems, it can be found that the edge modification can regulate the electronic structures and charge mobilities. Considering the edge states play an important role in the charge transport, the MoS_2 ribbon model of that one edge is terminated by F atoms and the other keeps pristine is investigated, which is denoted by F-p. In MoS_2 system, Mo atoms are donors and S atoms are acceptors. The H atoms termination can keep this relationship very well due to both of oxidability and reducibility in H atoms. But F atoms have very strong oxidability. The S-F bond (-3.5835eV) is much difficult to form than the F-Mo bond (-5.262475 eV). The model that only Mo atoms are terminated by X (F, Cl and Br) atoms (denoted by X-Mo) is investigated. As shown in Fig. 9, for F-p, electronic properties are major depended on the pristine edge. So there are the similar energy bands, deformation potential constants and mobilities can be observed. For X-Mo, there are indirect gaps in energy bands. The LUMO locates at Z point and HOMO locates at Γ point. This is similar as the mixture of pristine and F-termination. The $|E_1|$ is obviously getting small when Mo atoms are terminated by X atoms. In X-Mo, the μ_e is calculated which reach to 10^2 $cm^2V^{-1}s^{-1}$, which is almost three folds of that in pristine ribbons and two folds of that in monolayer MoS_2. The μ_h is calculated over 10^3 $cm^2V^{-1}s^{-1}$, which is at least one order of magnitude larger than that in monolayer MoS_2. These results suggest that the chemical modifactions on the MoS_2 ribbon edge can change the energy bands and promote the carries mobilities.

Conclusions

In summarily, we have calculated the electronic structures and the intrinsic charge carriers mobilities of MoS_2 sheet and nanoribbons with the effect of the longitudinal acoustic phonon, using first-principles density functional theory and the BTE with the relaxation time approximation. The numerical results indicate that the μ_h of sheet at room temperature, is about 96.62 $cm^2V^{-1}s^{-1}$, which is twice of μ_e (43.96 $cm^2V^{-1}s^{-1}$). While for the MoS_2 nanoribbons, the charge mobilities will be decreased obviously. The μ_e is about 30 $cm^2V^{-1}s^{-1}$ and μ_h is about 25 $cm^2V^{-1}s^{-1}$. Furthermore, we find that the edge modifcation can ehnace the mobilities in nanoribbons. The mobilities in H-termiantion nanoribbons are about 45 (electron) and 95 (hole) $cm^2V^{-1}s^{-1}$, and comparable to that in MoS_2 sheet. When edges are terminated by F atoms, the energy bands around Fermi level are seriously changed owing to the additonal p oribitals. The μ_e is 42.94 $cm^2V^{-1}s^{-1}$ (for N=16) and close to the results in MoS_2 sheet and H-termination ribbons. The μ_h increases to 425.20 $cm^2V^{-1}s^{-1}$ (for N=16) rapidly, which is at least one order larger than that in pristine ribbons. And when only the edge Mo atoms are terminated by halogen atoms, the μ_e will reach over 10^2 $cm^2V^{-1}s^{-1}$ and the μ_h will reach over 10^3 $cm^2V^{-1}s^{-1}$.

Acknowledgements

This work is supported by the National Natural Science Foundation of China (Grant Nos. 21103232, 61306149, and 11274260), the Natural Science Foundation of Hunan Province (No. 14JJ3026), Hong Kong Scholars Program (No. XJ2013003) and Shenghua Lieying Scholarship by the Central South University. It is also supported by Hunan Key Laboratory for Super-microstructure and Ultrafast Process and the Research Grants Council of Hong Kong SAR (Project No. CityU 100311/11P).

References

1 A. K. Geim and K. S. Novoselov, *Nat. mater.*, 2007, **6**, 183-191.

2 M. Long, L. Tang, D. Wang, Y. Li and Z. Shuai, *ACS Nano*, 2011, **5**, 2593-2600.

3 D. Jose and A. Datta, *Acc. Chem. Res.,* 2014, **47**, 593-602

4 M. P. Levendorf, C.-J. Kim, L. Brown, P. Y. Huang, R. W. Havener, D. A. Muller and J. Park,

Nature, 2012, **488**, 627-632.

5 V. Mohan and A. Datta, *J. Phys. Chem. Lett.* 2010, **1**, 136-140.

6 D. Jose and A. Datta, *Phys. Chem. Chem. Phys.,* 2011*,* **13***,* 7304-7311

7 M. Tahir and U. Schwingenschlogl, *Sci. Rep.*, 2013, **3**, 1075.

8 S. M. Jung, H. Y. Jung, M. S. Dresselhaus, Y. J. Jung and J. Kong, *Sci. Rep.*, 2012, **2**, 849.

9 Q. H. Wang, K. Kalantar-Zadeh, A. Kis, J. N. Coleman and M. S. Strano, *Nat. Nanotech.*, 2012, **7**, 699-712.

10 S. Yang, D. Li, T. Zhang, Z. Tao and J. Chen, *J. Phys. Chem. C*, 2012, **116**, 1307-1312.

11 Y. V. Joshi, P. Ghosh, P. S. Venkataraman, W. N. Delgass and K. T. Thomson, *J. Phys. Chem. C*, 2009, **113**, 9698-9709.

12 M. Remskar, A. Mrzel, M. Virsek, M. Godec, M. Krause, A. Kolitsch, A. Singh and A. Seabaugh, *Nanoscale Res. Lett.*, 2010, **6**, 26.

13 B. Radisavljevic, A. Radenovic, J. Brivio, V. Giacomett and A. Kis, *Nat. Nanotech.*, 2011, **6**, 147-150.

14 S. Kim, A. Konar, W. S. Hwang, J. H. Lee, J. Lee, J. Yang, C. Jung, H. Kim, J. B. Yoo, J. Y. Choi, Y. W. Jin, S. Y. Lee, D. Jena, W. Choi and K. Kim, *Nat. Commun.*, 2012, **3**, 1011.

15 C. Zhang, Z. Ning, Y. Liu, T. Xu, Y. Gao, A. Zak, Z. Zhang, S. Wang, R. Tenne and Q. Chen, *Appl. Phys. Lett.*, 2012, **101**, 113112.

16 F. L. Deepak, A. Mayoral and M. J. Yacaman, *Mater. Chem. Phys.*, 2009, **118**, 392-397.

17 F. L. Deepak, A. Mayoral, A. J. Steveson, S. Mejia-Rosales, D. A. Blom and M. Jose-Yacaman, *Nanoscale*, 2010, **2**, 2286-2293.

18 R. Kreizman, A. N. Enyashin, F. L. Deepak, A. Albu-Yaron, R. Popovitz-Biro, G. Seifert and R. Tenne, *Adv. Funct. Mater.*, 2010, **20**, 2459-2468.

19 G. Cunningham, M. Lotya, N. McEvoy, G. S. Duesberg, P. Schoot and J. N. Coleman, *Nanoscale*, 2012, **4**, 6260-6264.

20 L. Houben, A. N. Enyashin, Y. Feldman, R. Rosentsveig, D. G. Stroppa and M. Bar-Sadan, *J. Phys. Chem. C*, 2012, **116**, 24350-24357.

21 M. Ghorbani-Asl, S. Borini, A. Kuc and T. Heine, *Phys. Rev. B*, 2013, **87**, 235434.

22 C. Ataca, M. Topsakal, E. Akturk and S. Ciraci, *J. Phys. Chem. C*, 2011, **115**, 16354-16361.

23 K. F. Mak, C. Lee, J. Hone, J. Shan and T. F. Heinz, *Phys. Rev. Lett.*, 2010, **105**, 136805.

24 S. K. Mahatha, K. D. Patel and K. S. Menon, *J. Phys. Condens. Matter.*, 2012, **24**, 475504.

25 D. Xiao, G. B. Liu, W. Feng, X. Xu and W. Yao, *Phys. Rev. Lett.*, 2012, **108**, 196802.

26 T. Cheiwchanchamnangij and W. R. L. Lambrecht, *Phys. Rev. B*, 2012, **85**, 205302.

27 Z. Y. Zhu, Y. C. Cheng and U. Schwingenschlogl, *Phys. Rev. B*, 2011, **84**, 153402.

28 G. Kioseoglou, A. T. Hanbicki, M. Currie, A. L. Friedman, D. Gunlycke and B. T. Jonker, *Appl. Phys. Lett.*, 2012, **101**, 221907.

29 K. F. Mak, K. He, J. Shan and T. F. Heinz, *Nat. Nanotech.*, 2012, **7**, 494-498.

30 H. Zeng, J. Dai, W. Yao, D. Xiao and X. Cui, *Nat. Nanotech.*, 2012, **7**, 490-493.

31 T. Cao, G. Wang, W. Han, H. Ye, C. Zhu, J. Shi, Q. Niu, P. Tan, E. Wang, B. Liu and J. Feng, *Nat. Commun.*, 2012, **3**, 887.

32 Z. Gong, G. B. Liu, H. Yu, D. Xiao, X. Cui, X. Xu and W. Yao, *Nat. Commun.*, 2013, **4**, 2053.

33 S. Wu, J. S. Ross, G. B. Liu, G. Aivazian, A. Jones, Z. Fei, W. Zhu, D. Xiao, W. Yao, D. Cobden and X. Xu, *Nat. phys.* 2013, **9**, 149-153.

34 M. Q. Long, L. Tang, D. Wang, L. J. Wang and Z. G. Shuai, *J. Am. Chem. Soc.*, 2009, **131**, 17728-17729.

35 S. Bruzzone and G. Fiori, *Appl. Phys. Lett.*, 2011, **99**, 222108.

36 B. Xu, Y. D. Xiao, J. Yin, X. G. Wan, K. Jiang, A. D. Li, D. Wu and Z. G. Liu, *Appl. Phys. Lett.*, 2010, **96**, 183108.

37 G. Wang, *Phys. Chem. Chem. Phys.*, 2011, **13**, 11939-11945.

38 J. Xi, M. Long, L. Tang, D. Wang and Z. Shuai, *Nanoscale*, 2012, **4**, 4348-4369.

39 K. Kaasbjerg, K. S. Thygesen and K. W. Jacobsen, *Phys. Rev. B*, 2012, **85**, 115317.

40 K. Kaasbjerg, K. S. Thygesen and A.-P. Jauho, *Phys. Rev. B*, 2013, **87**, 235312.

41 X. Li, J. T. Mullen, Z. Jin, K. M. Borysenko, M. B. Nardelli, and K. W. Kim, *Phys. Rev. B*, 2013, **87**, 115418.

42 Y. Cai, Z. Gang and Y.-W. Zhang, *J. Am. Chem. Soc.*, 2014, **136**, 6269−6275.

43 R. Fivaz and E. Mooser, *Phys. Rev.*, 1976, **163**, 743-755.

44 K. S. Novoselov, D. Jiang, F. Schedin, T. J. Booth, V. V. Khotkevich, S. V. Morozov and A. K. Geim, *Proc. Natl. Acad. Sci. U.S.A.*, 2005, **102**, 10451–10453.

45 S. Najmaei, Z. Liu, W. Zhou, X. Zou, G. Shi, S. Lei, B. I. Yakobson, J.-C. Idrobo, P. M. Ajayan and J. Lou, *Nat. Mater.* 2013, **12**, 754−759.

46 B. Radisavljevic and A. Kis, *Nat. Mater.*, 2013, **12**, 815-820.

47 D. J. Late, B. Liu, H. S. S. R. Matte, V. P. Dravid, and C. N. R. Rao, *ACS Nano*, 2012, **6**, 5635-5641.

48 R. Wang, B. A. Ruzicka, N. Kumar, M. Z. Bellus, H.-Y. Chiu, and H. Zhao, *Phys. Rev. B*, 2012, **86**, 045406.

49 J. Wang, R. Zhao, M. Yang, Z. Liu and Z. Liu, *J. Chem. Phys.*, 2013, **138**, 084701.

50 X. Liu, T. Xu, X. Wu, Z. Zhang, J. Yu, H. Qiu, J.-H. Hong, C.-H. Jin, J.-X. Li, X.-R. Wang, L.-T. Sun and W. Guo, *Nat. Commun.*, 2013, **4**, 1776.

51 J. Xiao, M. Long, X. Li, H. Xu, H. Huang and Y. Gao, *Sci. Rep.*, 2014, **4**, 4327.

52 G. Nan, X. Yang, L. Wang, Z. Shuai and Y. Zhao, *Phys. Rev. B*, 2009, **79**, 115203

53 J. Bardeen and W. Shockley, *Phys. Rev.*, 1950, **80**,72−80.

54 W.-Q. Deng and W. A. Goddard III, *J. Phys. Chem. B*, 2004, **108**, 8614-8621.

55 G. Kresse and J. Furthmüller, *Comput. Mater. Sci.*, 1996, **6**, 15-50.

56 J. P. Perdew, K. Burke and M. Ernzerhof, *Phys. Rev. Lett.*, 1996, **77**, 3865-3868.

57 J. P. Perdew and Y. Wang, *Phys. Rev. B*, 1992, **45**, 13244-133278.

58 S. Bertolazzi, J. Brivio and A. Kis, *ACS Nano*, 2011, **5**, 9703−9709.

59 A. Castellanos-Gomez, M. Poot, G. A. Steele, H. S. J. van der Zant, N. Agraït and G. Rubio-Bollinger, *Adv. Mater.* 2012, **24**, 772−775.

60 Y. Zhang, J. Ye, Y. Matsuhashi and Y. Iwasa, *Nano Lett*., 2012, **12**,1136−1140.

61 A. Splendiani, L. Sun, Y. Zhang, T. Li, J. Kim, C.-Y. Chim, G. Galli, and F. Wang, *Nano. Lett.*, 2010, **10,** 1271-1275.

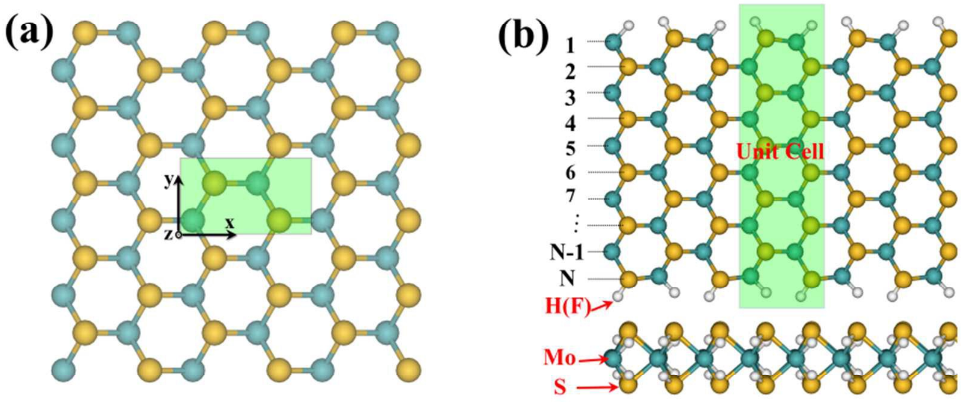

Fig. 1 The model of MoS_2 sheet (a) and nano-ribbons(b).

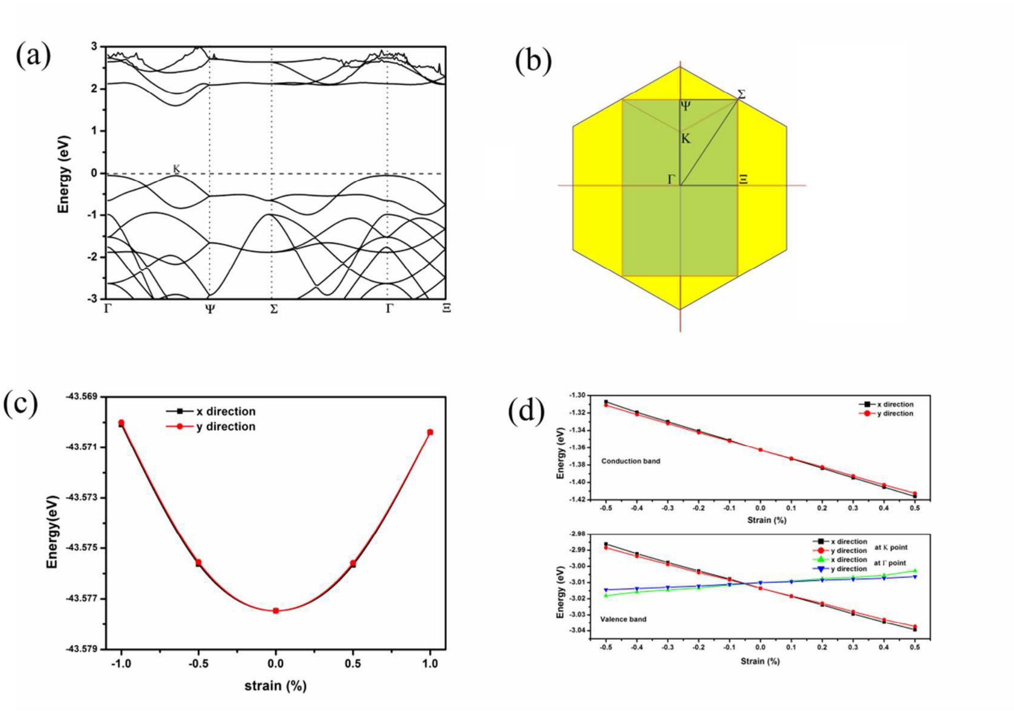

Fig. 2 Electronic properties of monolayer MoS_2 sheet. (a) Band structure for monolayer MoS_2 sheet with the orthogonal supercell shown in Fig. 1(a). (b) The first Brillouin zone (c) Energy−strain relationship along the x and y directions. (d) Shifts of the conduction band and valence band edges under an uniaxial strain.

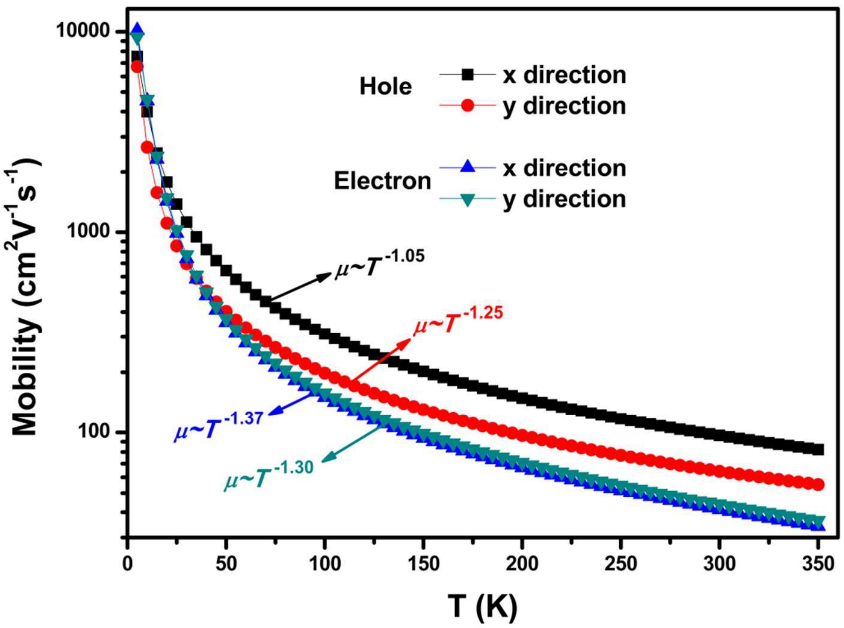

Fig. 3 The mobility as a function with temperature in MoS_2 sheet.

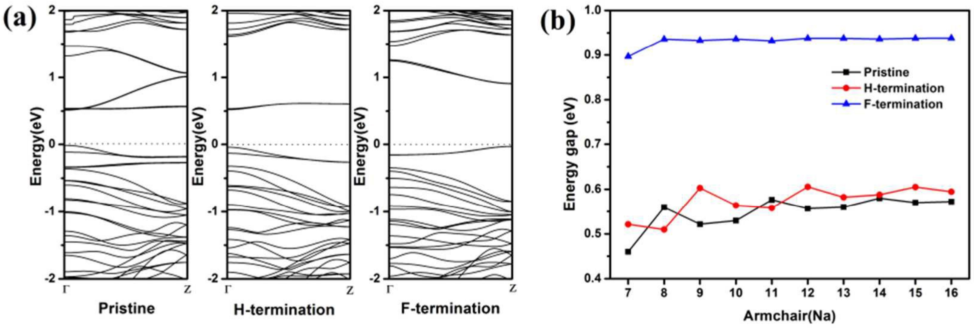

Fig. 4 (a) the band structure of an armchair nanoribbon (*Na*=10) and (b) the energy gap of armchair nanoribbon as a function with width(*Na*).

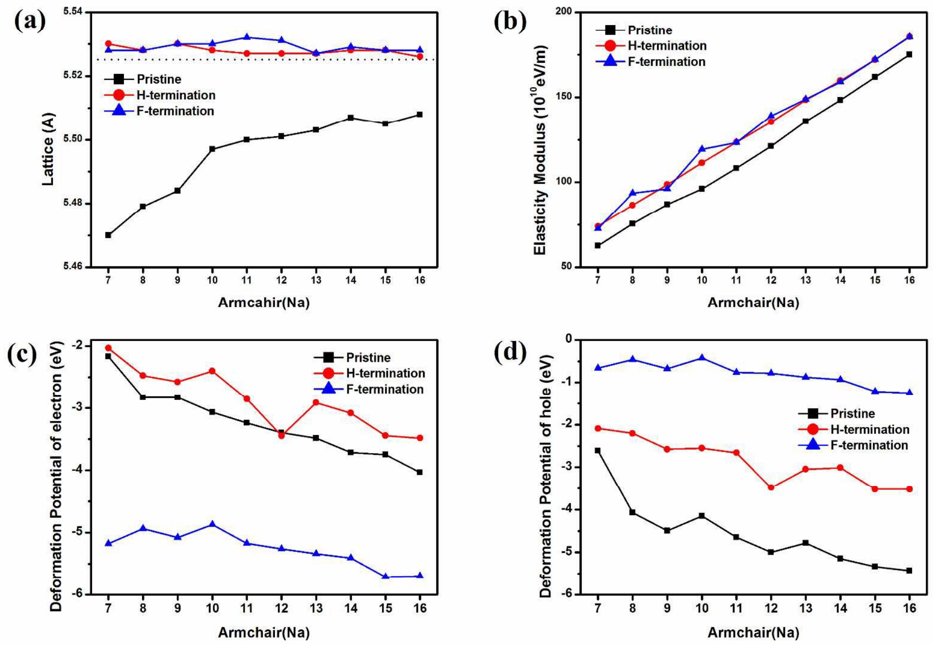

Fig. 5 The lattice length (a), elasticity modulus (b) and deformation protential of electron(c) and hole (d) in armchair nanoribbon.

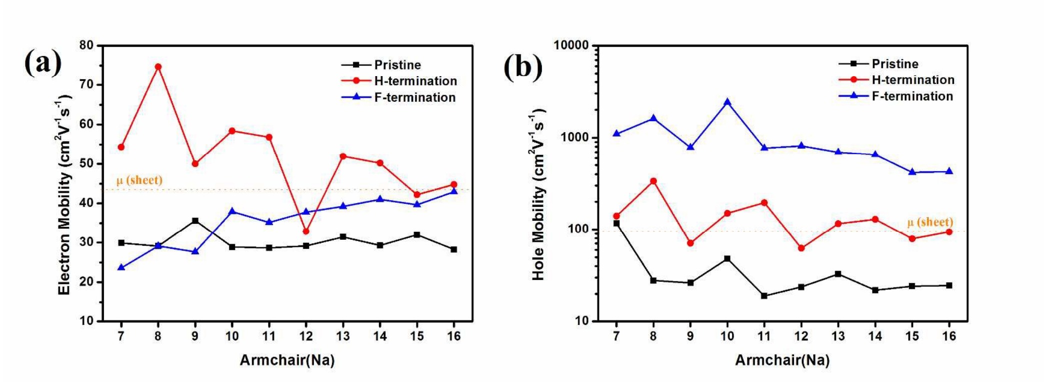

Fig. 6 The mobility of electron (a) and hole (b) in armchair nanoribbons. The dot line is the mobility of monolayer MoS_2 predicted by BTE method.

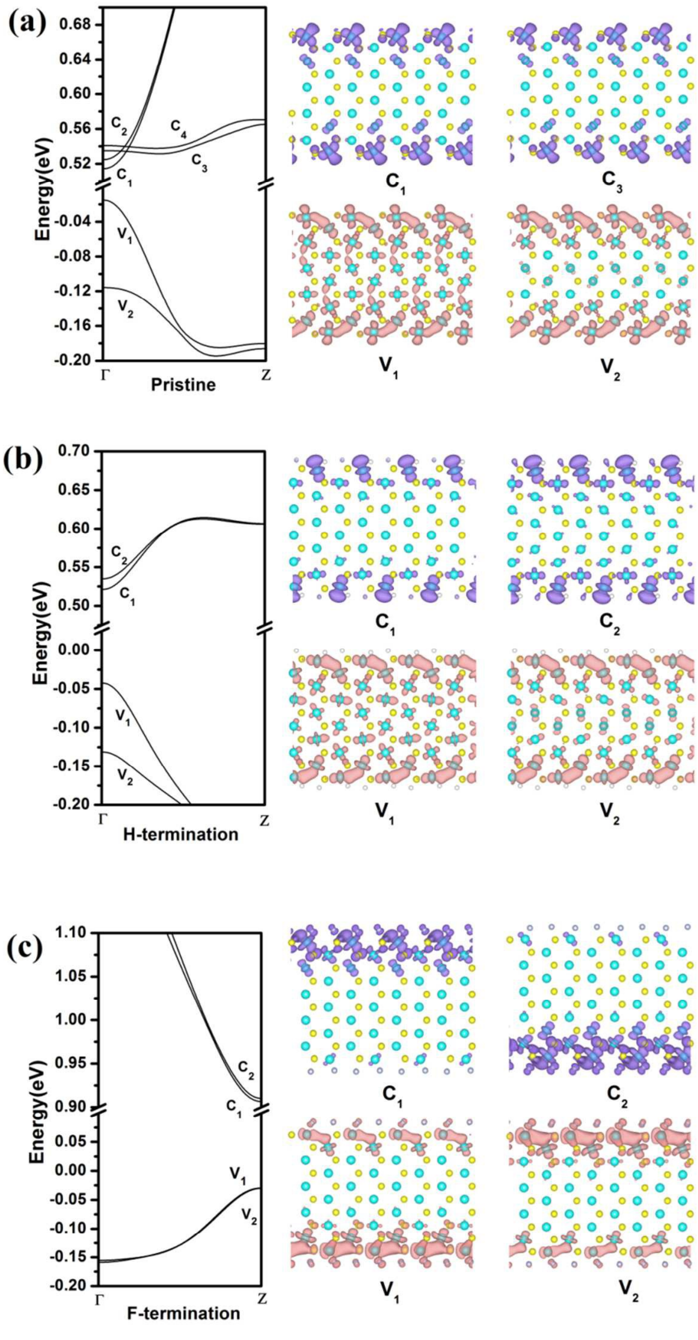

Fig. 7 Band decomposed charge density of MoS_2 nanoribbons with Na=10: (a) pristine ribbon; (b) H atoms termination ribbon; (c) F atoms termination ribbon. The Fermi level is set to zero.

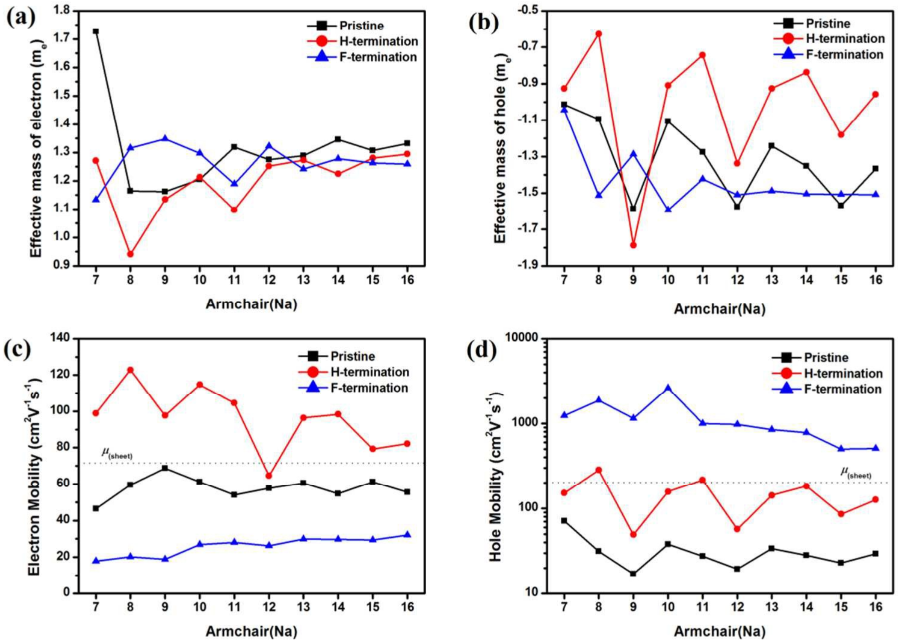

Fig. 8 The effective mass of MoS_2 ribbons, and the mobility based on effective mass method. (a) effective mass of electron; (b) effective mass of hole; (c) the mobility of electron obtained by effective mass; (d) the mobility of hole obtained by effective mass. m_e is the mass of free electron. The dot lines are the mobility of monolayer MoS_2 which are 72.16 (electron) and 200.52 (hole) $cm^2V^{-1}s^{-1}$ reported in Ref.[42].

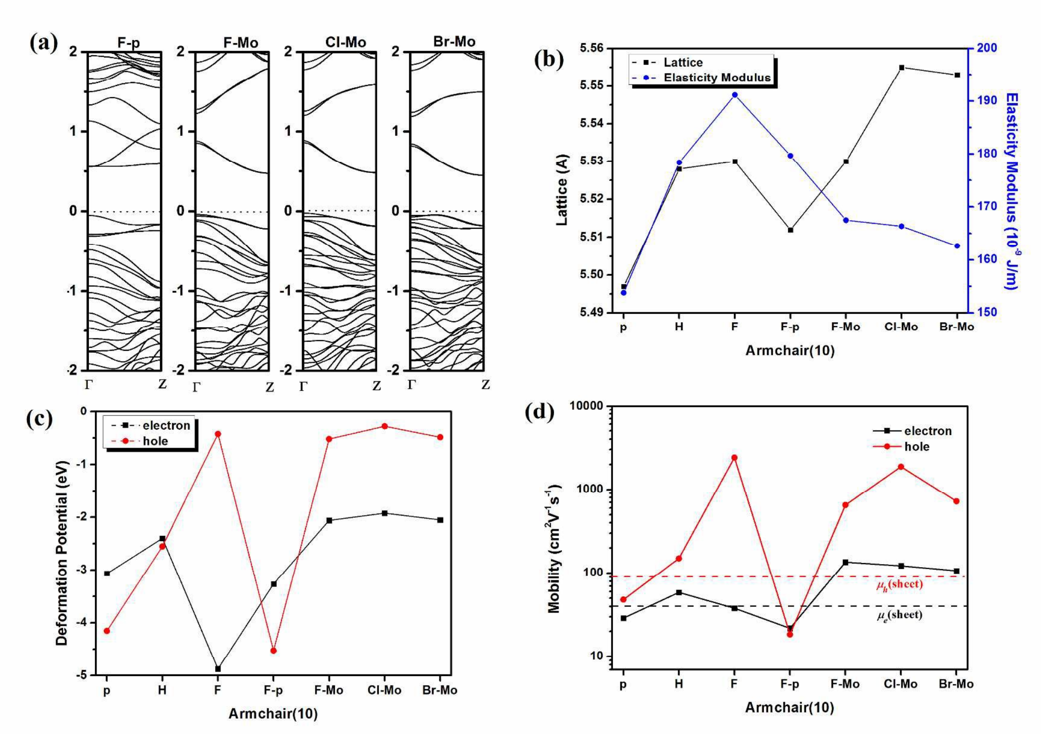

Fig. 9 (a)The band structures of armchair (10) with different edge modification; (b) the lattice length and elasticity modulus; (c) the deformation potential(E_1); (d) the mobility calculated by the BTE method. The pristine ribbon in denoted by p. Both of the two edges terminated by H atoms or F atoms are denoted by H or F. The ribbon with only one edge terminated by F atoms marks as F-p. The model of only Mo atoms terminated by X (F, Cl and Br) atoms is denoted by X-Mo. The red (black) dashed line is the hole (electron) mobility of monolayer MoS_2 calculated by the BTE method.

Table 1 Deformation potential E_1, in-plane stiffness C^{2D}, relaxation time τ, and mobility μ for electron (e) and hole (h) along the x and y directions in a 2D monolayer MoS_2 sheet at 300 K.

Carrier type	direction	E_1(eV)	C^{2D}(N/m)	τ (fs)	μ ($cm^2V^{-1}s^{-1}$)	μ* ($cm^2V^{-1}s^{-1}$)
e	x	-10.80	131.31	14.88	41.27	72.16
	y	-10.68	131.47	15.22	43.96	60.32
h	x (K)	-5.28	131.31	52.15	96.62	200.53
	y (K)	-5.22	131.47	53.56	64.19	152.18
	x (Γ)	1.31	131.31	1229.16	3079.39	-
	y (Γ)	0.82	131.47	3125.25	4973.83	-

μ* the mobility reported in Ref. 42.